Supporting Information

Table S1. Statistics of the leading singular value decomposition (SVD) modes of sea surface temperatures (SST) and sea level pressures (SLP) in spring (MAM) and summer (JJA) over a region encompassing the northeast Pacific Ocean, North America, and the northern Atlantic Ocean (160°W-20°W, 0-60°N). Data are from the National Centers for Environmental Prediction (NCEP) for 1948-2013.

	MAM variance (%)	JJA variance (%)	Spatial covariance of MAM and JJA (%)	Temporal correlation of determination (R^2) between MAM and JJA
SST mode1	27.9	18.4	52.6	80.0
SST mode2	11.9	18.7	23.7	82.7
SLP mode1	19.2	24.5	51.9	48.4

Table S2. Models from the Coupled Model Intercomparison Project Phase 5 (CMIP5) used for this study.

Model Name	Institute
ACCESS1.0	Commonwealth Scientific and Industrial Research,Organization (CSIRO) and Bureau of Meteorology (BOM), Australia
ACCESS1.3	Commonwealth Scientific and Industrial Research,Organization (CSIRO) and Bureau of Meteorology (BOM), Australia
BCC-CSM1-1	Beijing Climate Center, China Meteorological Administration
BNU-ESM	College of Global Change and Earth System Science, Beijing Normal University
CanAM4	Canadian Centre for Climate Modelling and Analysis
CCSM4	National Center for Atmospheric Research
CESM1	Community Earth System Model Contributors
CMCC-CM	Centro Euro-Mediterraneo per i Cambiamenti Climatici
CNRM-CM5	Centre National de Recherches Météorologiques / Centre Européen de Recherche et Formation Avancée en Calcul Scientifique
CSIRO-MK3-6-0	Commonwealth Scientific and Industrial Research Organization in collaboration with Queensland Climate Change Centre of Excellence
EC-EARTH	EC-EARTH consortium
FGOALS-g2	LASG, Institute of Atmospheric Physics, Chinese Academy of Sciences
FGOALS-s2	LASG, Institute of Atmospheric Physics, Chinese Academy of Sciences
GFDL-CM3	NOAA Geophysical Fluid Dynamics Laboratory
GFDL-HIRAM-C180	NOAA Geophysical Fluid Dynamics Laboratory
GISS-E2-R	NASA Goddard Institute for Space Studies
HadGEM2-A	Met Office Hadley Centre (additional HadGEM2-ES realizations contributed by Instituto Nacional de Pesquisas Espaciais)
INMCM4	Institute for Numerical Mathematics
IPSL-CM5A-LR	Institut Pierre-Simon Laplace
IPSL-CM5A-MR	Institut Pierre-Simon Laplace
IPSL-CM5B-LR	Institut Pierre-Simon Laplace
MIROC-ESM	Japan Agency for Marine-Earth Science and Technology, Atmosphere and Ocean Research Institute (The University of Tokyo), and National Institute for Environmental Studies
MIROC5	Atmosphere and Ocean Research Institute (The University of Tokyo), National Institute for Environmental Studies, and Japan Agency for Marine-Earth Science and Technology
MPI-ESM-LR	Max-Planck-Institut für Meteorologie (Max Planck Institute for Meteorology)
MPI-ESM-MR	Max-Planck-Institut für Meteorologie (Max Planck Institute for Meteorology)
MRI-AGCM3-2H	Meteorological Research Institute
MRI-CGCM3	Meteorological Research Institute
NORESM1-M	Norwegian Climate Centre

1. **The first empirical orthogonal function (EOF) of June-July-August (JJA) maximum daily 8-hour (MDA8) ozone concentrations across the eastern United States.**

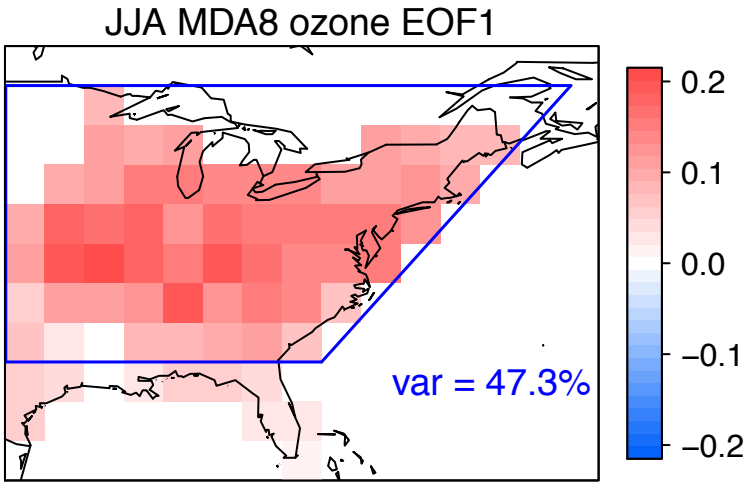

Fig. S1. The first EOF loading of JJA mean MDA8 ozone from 1980 to 2013 across the eastern United States. Shown inset is the variance explained by the EOF pattern. In calculating the relationships of JJA ozone with springtime meteorological variables, we define the eastern United States as the region within the blue quadrangle (100°W-65°W, 31°N-50°N), and we refer to JJA ozone in this region as East-JJA-O_3. Gridboxes south of 31°N are not included in this definition because our model has little predictive value in this region.

2. Spatial loadings of the singular value decomposition (SVD) modes of SST and SLP in spring and summer

A key question is whether the correlations of East-JJA-O_3 with SST or SLP reflect the influence of major large-scale weather patterns that explain much of the climate variability in North America and the adjacent oceans. To examine this issue, we analyze the covariance of spring SSTs with summer SSTs within a large spatial domain (160°W-20°W, 0°N-60°N) that includes the northeast Pacific, North America, and the northern Atlantic. We perform the analysis by applying singular value decomposition (SVD) to 1948-2013 SSTs, and we do the same analysis for SLPs. We change the timeframe from 1980-2013 to 1948-2013 to provide greater statistical significance to our results. Before performing SVD, we scale the time series of SLP or SST in each grid box to achieve zero mean and unit standard deviation. Table S1 summarizes the statistics for the variance explained by each mode and the temporal correlation between the time series of principal components (PC).

For SST, the first SVD mode explains 52.6% of the covariance between spring and summer, characterized by warm SSTs extending across the tropics and along the west coast of North America and by cold SSTs in the central northern Pacific and Atlantic (Fig. S2a-b). The time series for this mode in the two seasons correlates with a high coefficient of determination (R^2 =0.80), suggesting that the observed SVD pattern in spring likely persists through summer and provides a source of seasonal predictability. Fig. S2c-d show the spatial loadings of the second SVD pattern of SST in spring and summer, which explains 23.7% of the covariance, featuring negative values in the eastern Pacific Ocean and positive values in the Atlantic. The time series of the second mode between spring and summer also shows high correlation (R^2 = 0.83). Together these first two modes explain 76.3% of the covariance between the spring and summer patterns in SST over the domain. A closer look reveals that the observed correlations of East-JJA-O_3 and SST (Fig. 1b) represent a combination of these two SST SVD patterns. The positive correlations over tropical Atlantic in Fig. 1b are found in the first mode of SST (Fig. S2a-b), while the negative correlations over the northeast Pacific are found in the second mode of SST (Fig. S2c-d). Then we use a linear regression model to regress the correlations of East-JJA-O_3 and MAM SST (y) in each grid box (Fig. 1b) onto the spatial loadings of the two SST SVD modes (x_1, x_2) in MAM (Fig. S2a,c). The model is of the form

$$y = k_1 x_1 + k_2 x_2 + b$$

where k_1 and k_2 are the regression coefficients, and b is the intercept. We find these two SST SVD modes can explain 60.3% of the spatial patterns of correlations between East-JJA-O_3 and MAM SST.

For SLP, the first SVD pattern explains 51.9% of the covariance between the spring and summer. The SLP pattern (Fig. S2e-f) features positive anomalies in the tropical and central Pacific but negative anomalies extending in a broad swath from the tropical and central Atlantic across North America to the northern Pacific Ocean. Similar to the SST SVD analysis, we regress the correlations between East-JJA-O_3 and SLP in Fig. 1e onto the spatial loading of the first SLP SVD mode in MAM (Fig. S2e). The coefficient of determination (R^2) is 79.6%, suggesting a high similarity between these two patterns. The time series for this SVD mode in spring and summer also shows relatively high correlation (R^2=0.48). To explore the relationship of SLP and SST, we regress the time series of the first SLP mode onto the time series of the first two SST modes in spring. We find the two SST modes can together explain almost 60% of the total

variability in the first SLP mode for 1948-2012, suggesting that the SLP and SST anomalies are closely linked.

Comparing Fig. 1 and S2 reveals that: (1) the observed SVD patterns of both SST and SLP in spring likely persist through summer (Fig. S2), providing a source of seasonal predictability; (2) the observed correlations of East-JJA-O3 and SST (Fig. 1b) represent a combination of the first two SST SVD patterns (Fig. S2a,c), with the positive correlations in North Atlantic found in the first SST SVD mode (Fig. S2a) and negative correlations over the northeast Pacific identified in the second SST SVD mode (Fig. S2b); (3) the correlation between East-JJA-O_3 and SLP (Fig. 1e), which displays a significant east-west contrast in the eastern Pacific and North America, is also found in first SLP SVD pattern (Fig. S2e). Therefore, we infer that the observed influence of SST and SLP on East-JJA-O_3 actually reflects the variability of atmospheric circulations over a much larger domain, including the northeast Pacific, North America, and the North Atlantic.

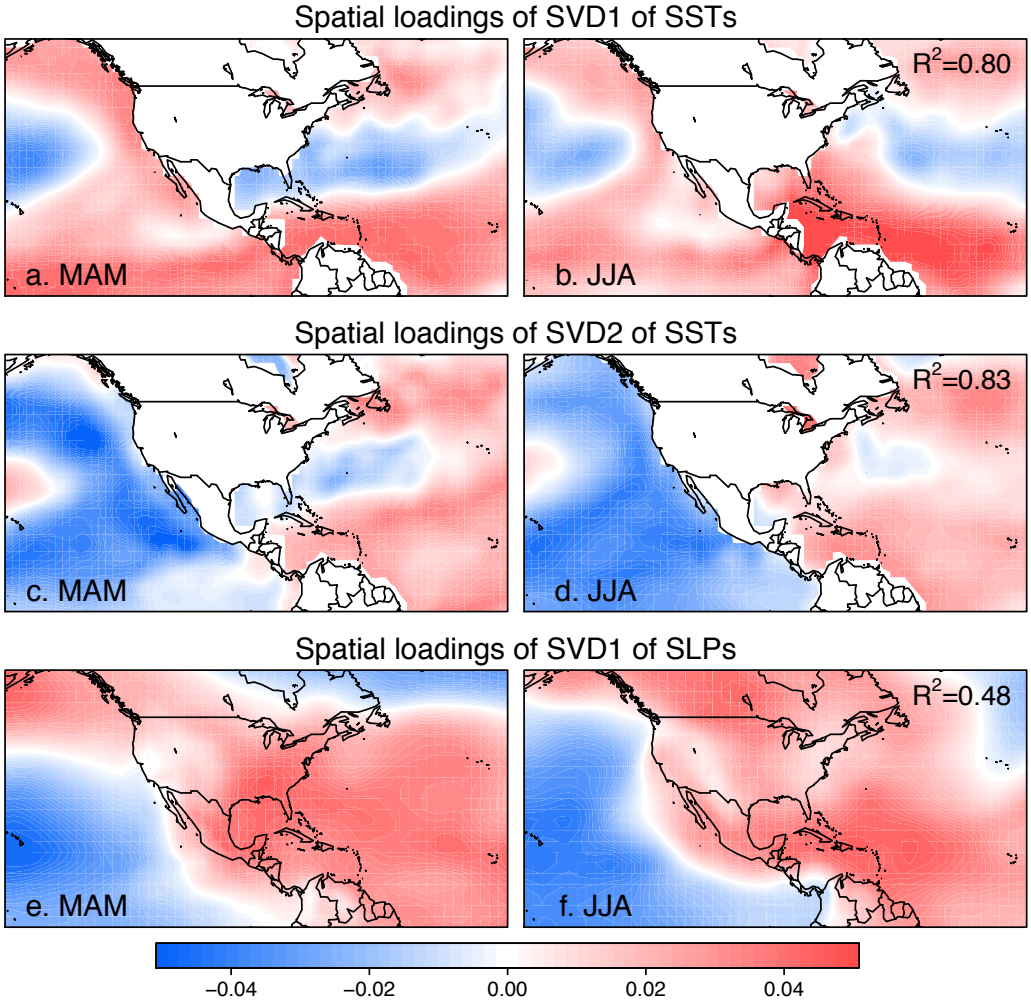

Fig. S2. Spatial loadings of the first SVD mode (SVD1) of SSTs in (a) spring and (b) summer over 1948-2013. Number inset in panel (b) is the coefficient of determination (R^2) for the time series of the principal components (PC1) of SST SVD1 for these two seasons. Other panels are the same as panels (a-b), but for the second SVD mode of SSTs (c-d) and the loadings of the first SVD mode of SLP (e-f).

3. Correlation of JJA ozone and 500 hPa geopotential heights in the months leading up to and including summer

We also explore potential teleconnections in the mid-troposphere with East-JJA-O_3 that link the SST and/or SLP patterns to East-JJA-O_3. Fig. S3 shows the correlation of JJA ozone and 500 hPa geopotential heights in the seasons leading up to and including summer. In MAM, the spatial pattern of the correlation coefficient *r* displays a tripole mode with positive correlations over low (~0-20°N) and high (~55°N-70°N) latitudes but negative correlations in the region between. To characterize this pattern, we define MAM-Δgph as the average geopotential height difference between northeastern Canada (region 2 in Fig. S3b) across the northeastern Pacific and the western United States (region 1 in Fig. S3b) in spring. This springtime pattern evolves into a teleconnection wave chain by summer with a high-pressure ridge centered over the eastern United States, concurrent with high ozone anomalies (Fig. S3c).

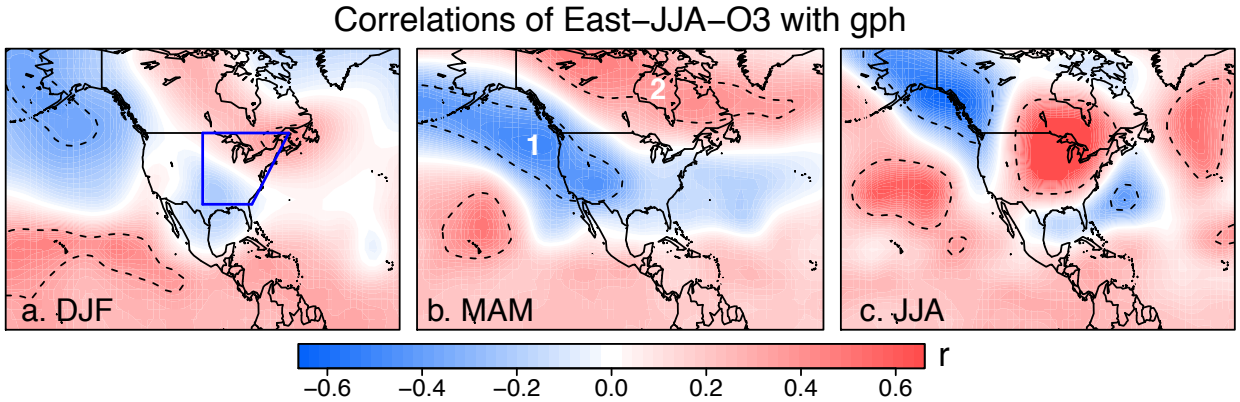

Fig. S3. Correlation of June-July-August (JJA) MDA8 ozone in the eastern United States with 500 hPa geopotential heights (gph) averaged over three-month intervals in the seasons leading up to and including summer for 1980-2013. We define East-JJA-O_3 as the mean summertime ozone averaged over the blue quadrangle in panel (a) and the MAM-Δgph index as the average difference in MAM 500 hPa geopotential heights between region 1 in the western United States and region 2 in the eastern Canada (panel b). The dashed contour lines enclose regions in which the correlations are statistically significant (p=0.05).

4. Singular value decomposition (SVD) analysis of 500 hPa geopotential heights in spring and summer.

Here we use SVD analysis to examine the links between 500 hPa geopotential heights and surface ozone (Fig. S4). In spring, the first mode of 500 hPa geopotential heights resembles the correlation pattern of East-JJA-O_3 and these heights at that time of year (Fig. S3b), while in summer, the first mode of 500 hPa geopotential heights shows a wave chain similar to the one in the correlation between East-JJA-O3 and these heights in that season (Fig. S3c). In addition, the spring and summer time series for this mode show relatively high correlation (R^2=0.46), indicating that 500 hPa geopotential heights can also provide a source of seasonal predictability. In spring, the correlation coefficient r is 0.51 between the time series of the first SVD mode of gph and SLP, and 0.90 between gph and SST, suggesting that this mid-tropospheric teleconnection pattern is likely related to both SST and SLP patterns.

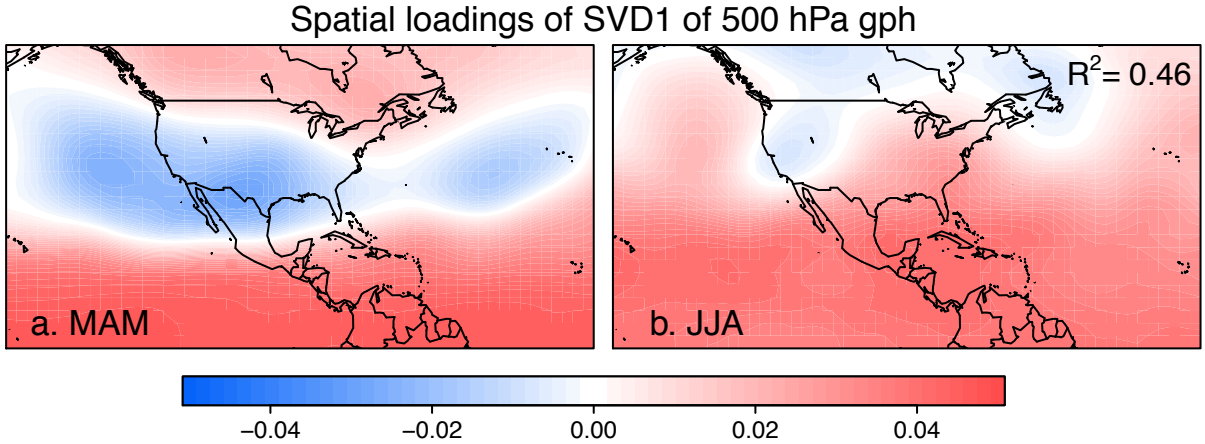

Fig. S4. Spatial loadings of the first SVD mode (SVD1) of 500 hPa geopotential heights in (a) MAM and (b) JJA over 1948-2013. Shown inset in panel (b) is the coefficient of determination (R^2) for the two timeseries of the principal components (PC1) of SVD1 for these seasons.

5. Prediction of summertime ozone episodes using SSTs and 500 hPa geopotential heights.

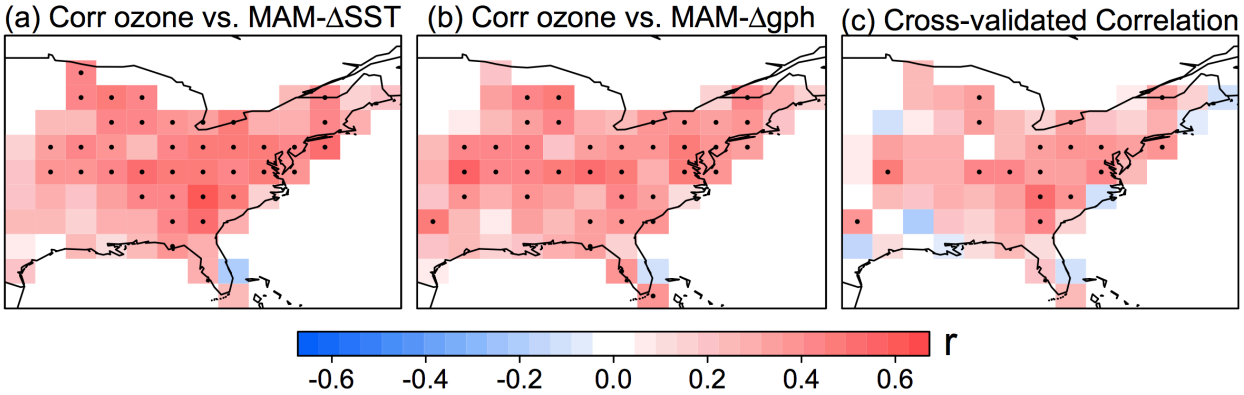

Fig. S5: Correlation of JJA ozone episode days in each gridbox with (a) MAM-ΔSST and (b) MAM-Δgph indices for 1980-2013. An episode is defined as a day with MDA8 ozone greater than 70 ppb. (c) Cross-validated correlation coefficient *r* between observed mean JJA ozone episode days and those modeled using either the MAM-ΔSST and MAM-Δgph indices or a combination of both. The episode timeseries has been detrended by subtracting the 7-year moving average. In all panels, gridboxes with significant correlations are stippled ($p < 0.05$). See text for more details.

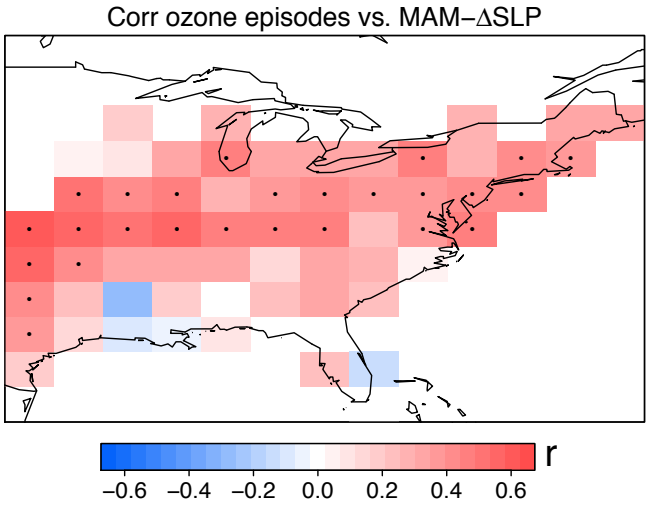

Fig. S6. Similar as Fig. S5a-b, but for the MAM-ΔSLP.

6. Prediction of summertime ozone episodes using SSTs and 500 hPa geopotential heights.

We also investigate the potential of our approach to predict the number of JJA ozone episodes, which we define as days each summer when MDA8 ozone exceeds 70 ppbv. We use the same regression method as above but replace MAM-ΔSLP with MAM-Δgph since MAM-Δgph is better correlated with ozone episodes than MAM-ΔSLP (Fig. S5-6). We find that JJA ozone episodes show significant positive correlations with both MAM-ΔSLP and MAM-Δgph in the Northeast and Midwest, but weak correlations in the deep South (Fig. S5a-b). Using the same approach as for East-JJA-O_3 yields a correlation coefficient r between the observed and predicted ozone episodes of ~0.5 in part of the Northeast, Southeast and Midwest, but less elsewhere (Fig. S5c). For the 1980-2013 time series of ozone episode number averaged over the eastern United States, we find correlations between observations and predictions of 0.52-0.55, depending on the detrending method (Fig. S7). Thus the model can predict as much as 30% of the variability in summertime ozone episodes in spring. Given the nonlinear response of daily MDA8 ozone to chemistry and meteorology, the capability to capture even one-third of the interannual variability of ozone episodes is encouraging. In response to air quality regulations, the number of ozone episodes per summer has largely decreased since 1980, leading to lower variance of interannual ozone episodes in the recent years, as seen in Fig. S7. We therefore have much better correlation coefficient r in the timeframe with high variance of ozone episodes, with r = 0.90 in 1980-1995 and r = 0.15 in 1996-2013 using HF, and r = 0.79 in 1980-1995 and r = 0.22 in 1996-2013 using MA. Our result suggests that the relationship of ozone episodes and meteorology is very sensitive to different anthropogenic emission levels. The predicative capability of ozone episodes could likely be improved with a longer timeseries of observations under a relative constant emission level.

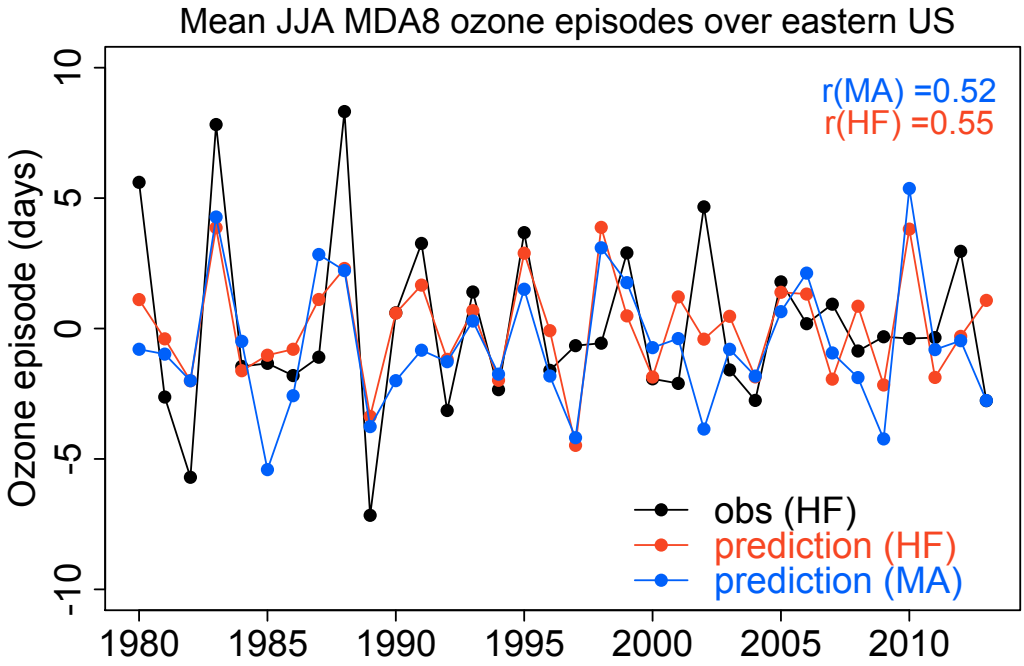

Fig. S7. Timeseries of observed and modeled mean JJA MDA8 ozone episodes (> 70 ppbv), averaged over the eastern United States (100°W-65°W, 31°N-50°N). Observations are shown in black, and are detrended using 7-year Henderson moving averages (HF). The red curve denotes the modeled values detrended using HF, while the blue curve indicates modeled values detrended using the 7-year moving average (MA). The correlations *r* of the two modeled timeseries with that observed are shown inset.

7. Correlation of MAM SSTs and MAM meteorological variables

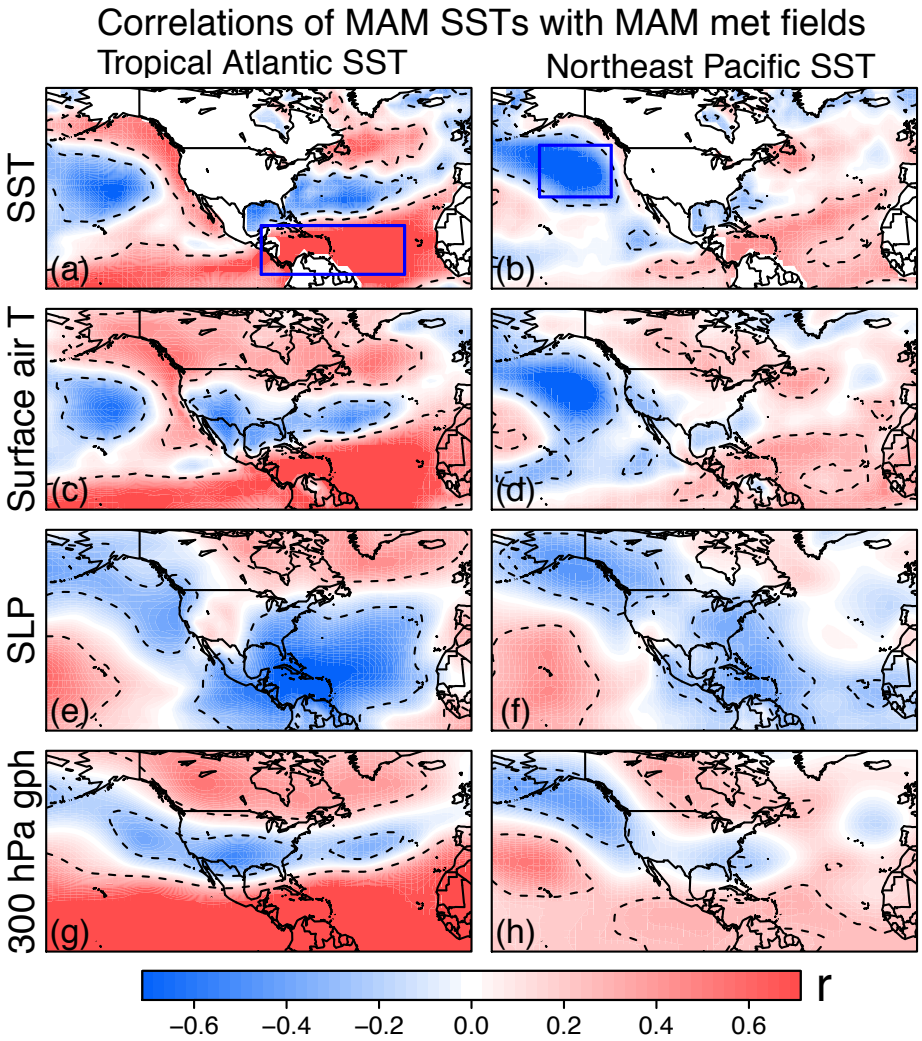

Fig. S8. Same as Fig. 4, but for the meteorological variables in spring.

8. Correlations of MAM SSTs in tropical Atlantic with other JJA meteorological factors

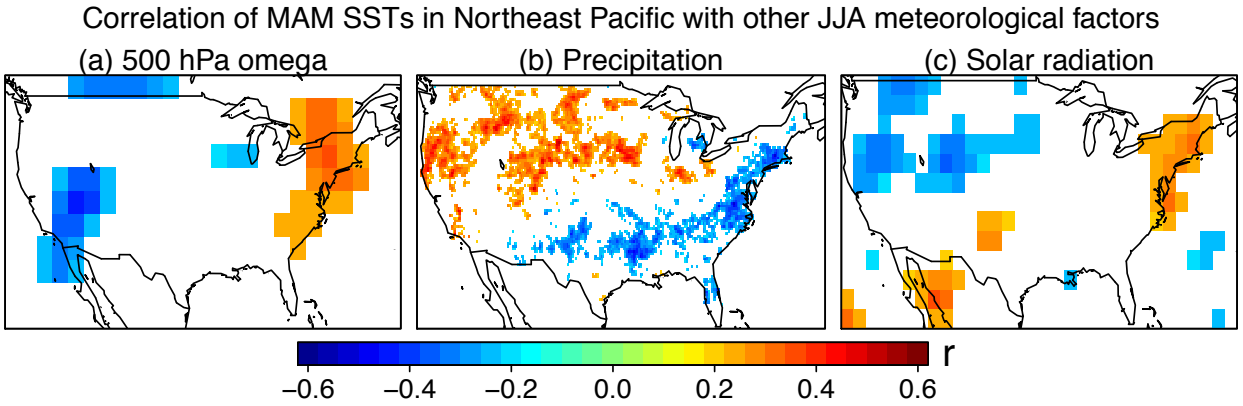

Fig. S9. Correlation of mean MAM tropical Atlantic SSTs (denoted as the blue rectangle in Fig. 4a) with JJA mean (a) 500-hPa omega (i.e., vertical velocity in Pa s^{-1}), (b) precipitation, and (c) surface solar radiation over 1948-2013. Shaded regions are significant at the 90% level. Positive values in panel (a) denote subsidence. All data are detrended by subtracting the 7-year moving averages. Omega and solar radiation are obtained from NCEP Reanalysis 1. Precipitation is from Climate Prediction Center U.S. Unified Precipitation data (1, 2).

9. Correlations of MAM SSTs and SLPs in different regions with East-JJA-O3

Figure S10 displays the correlation of the East-JJA-O_3 with four different predictors, including SSTs in the northeast Pacific and tropical Atlantic as well as SLPs in central Pacific and North America, in the preceding spring for 1980-2013. Based on previous studies (3-6) and our correlation analysis, the tropical Atlantic Ocean can trigger the large-scale meteorological patterns that enhance the ozone concentration in the eastern United States, while the northeast Pacific is more likely to respond to large-scale atmospheric variability rather than to serve as a "trigger" to such variability. (See main text for more details on correlation analysis.) However, as seen from the figure, the Northeast Pacific SSTs exhibit the strongest correlations with East-JJA-O_3 among these four predictors, which can be explained as follows. The atmospheric variability that influences ozone concentrations in the eastern United States consists of two sources: one follows the variability of northern tropical Atlantic SSTs (Fig. 4), and the other arises from atmospheric internal variability or other processes. By responding to both these types of atmospheric variability, the northeast Pacific SSTs may explain more variability of ozone in the eastern United States than northern tropical Atlantic SSTs. We formulate this hypothesis, however, on a relative short history (~34 years) of ozone observations, and there is some uncertainty in our conclusion.

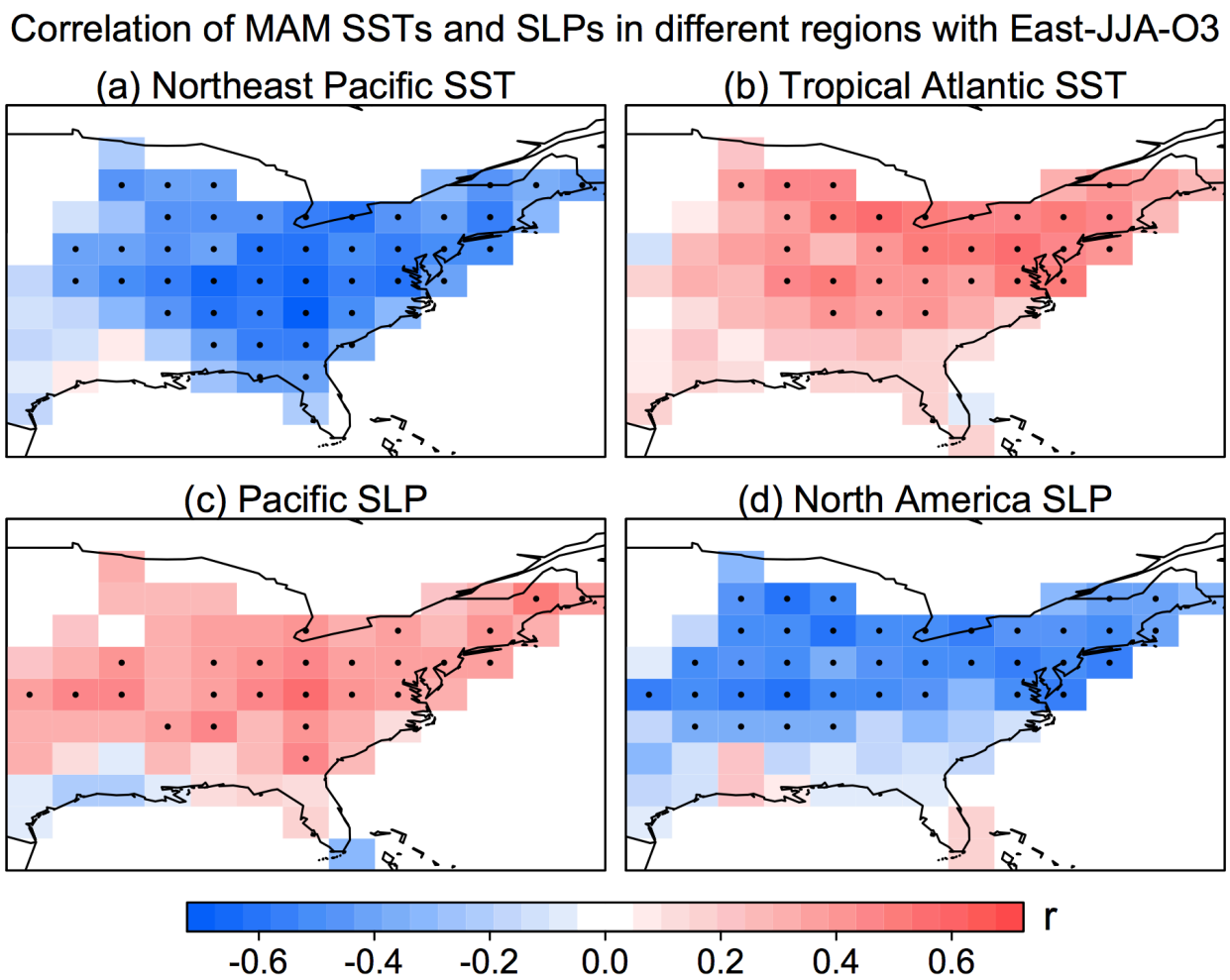

Fig. S10. The correlations of summertime MDA8 ozone in the eastern United States with MAM (a) northeastern Pacific SSTs (red rectangle in Fig. 1b), (b) northern tropical Atlantic SSTs (black rectangle in Fig. 1b), (c) central Pacific SLPs (black rectangle in Fig. 1e), and (d) North America SLPs (red rectangle in Fig. 1e). All data are detrended by subtracting the 7-year moving averages. In all panels, gridboxes with statistically significant ($p < 0.05$) correlations are stippled.

10. EOF analysis of the Northeast Pacific SST

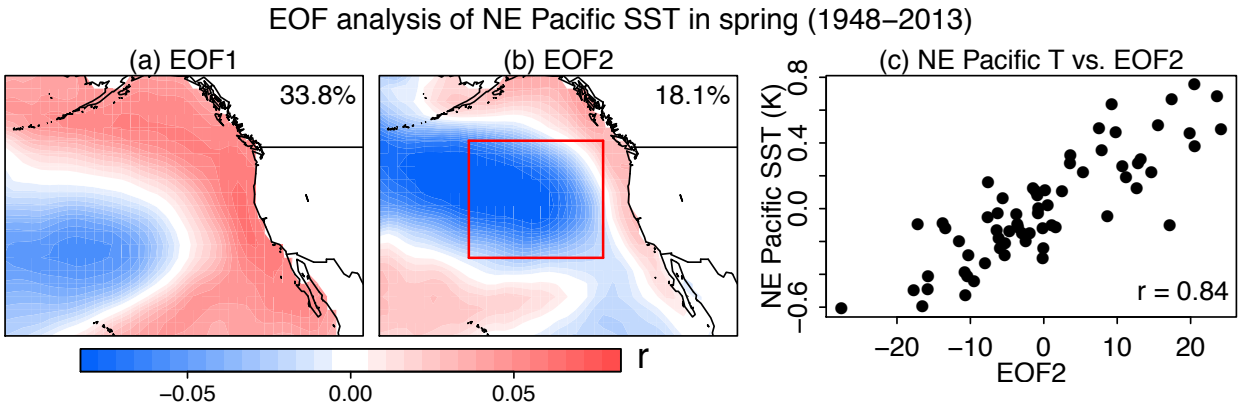

Fig. S11. (a-b) The first two EOF patterns of mean MAM SSTs for 1948-2013 in the Northeast Pacific (180°W-100°W, 20°N-60°N). Before performing EOF analysis, we scale the time series of SST in each grid box to achieve zero mean and unit standard deviation. The red rectangle in panel b is same as the one in Fig. 1b, which is used to predict the summertime ozone in the eastern United States. The variances in surface temperature explained by each EOF mode are shown inset. (c) Scatter plot of the EOF2 time series and average anomalies in the central Northeast Pacific SSTs (red rectangle in panel b), with the correlation coefficient inset.

11. Correlations of JJA surface temperatures in the eastern United States with SSTs in each AMIP model

To evaluate the capability of climate models to capture the observed links between mean JJA temperatures in the eastern United States and patterns in SSTs, we analyze the correlations in one simulation in the suite of simulations available for each AMIP model. We arbitrarily chose the "r1i1p1" simulation – i.e., **r**ealization 1, **i**nitialization method 1, and **p**erturbed physics 1. Our approach does not represent a rigorous evaluation of any particular model since each model may perform differently with different initializations and physical conditions. But taken together, the ensemble results likely reveal some common features in these models. Using observations, Fig. 5a shows that the correlations of JJA surface air temperatures in the eastern United States with SSTs in spring display a spatial pattern similar to that for ozone in Fig. 1b, with a tripole mode in the Atlantic and negative correlations in the northeast Pacific and U.S. west coast. However, only a few AMIP models (CanAM4, CSIRO-Mk3-6-0, EC-EARTH and MRI-AGCM3-2H) can capture the observed pattern (Fig. S12). In summer, observations show that the region with negative correlations expands in the Pacific (Fig. 5b), representing the Pacific extreme pattern that is associated with more heatwaves in the eastern United States (7). Most AMIP models can simulate the positive correlations in the Atlantic and negative correlations in the Pacific, but the correlations are much weaker than those in the observations (Fig. S13). Our results suggest that it is challenging for climate models to capture these seasonally evolving teleconnections related to summer temperatures in the eastern United States. Reasons for this difficulty are unclear.

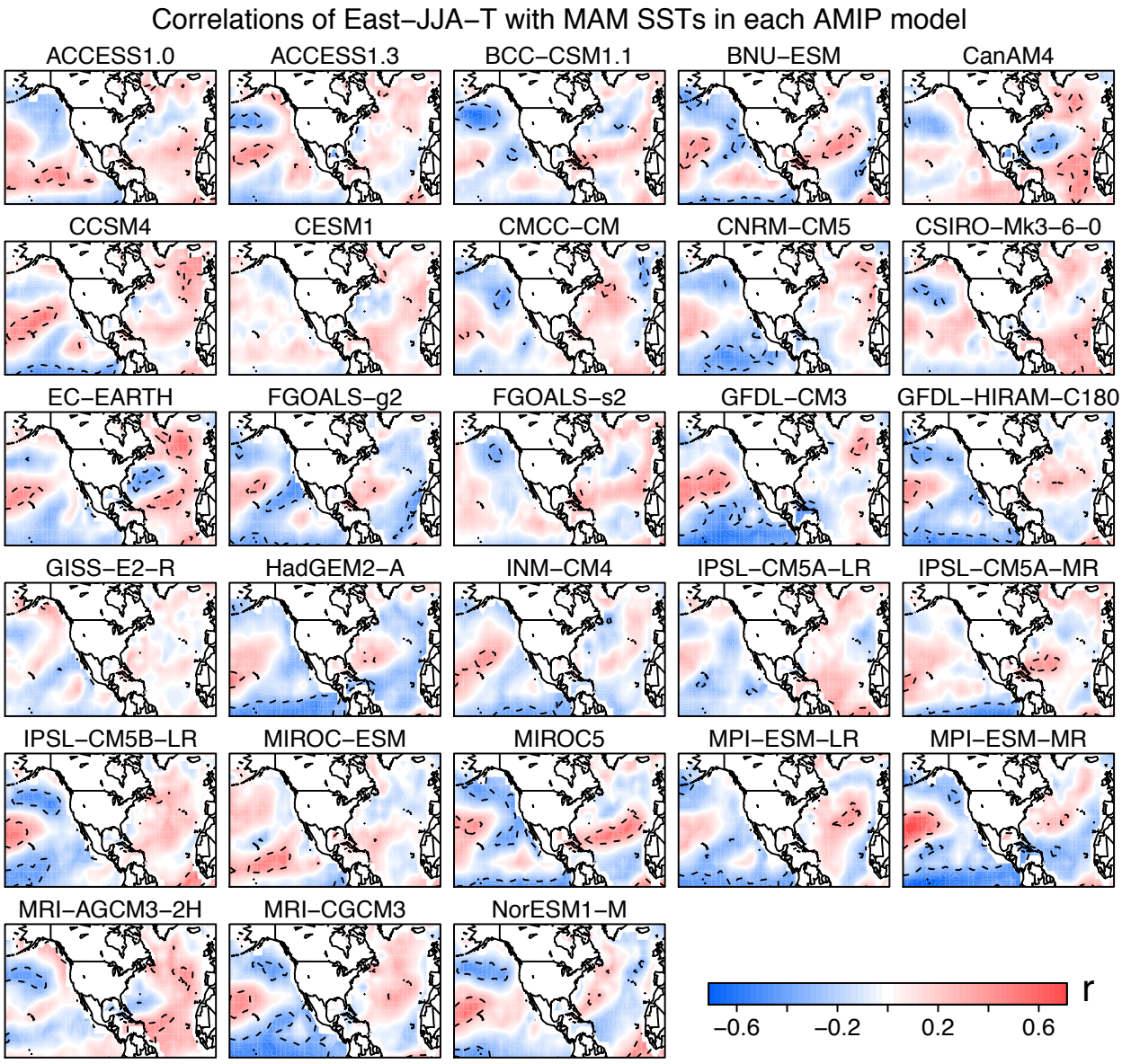

Fig. S12. Correlations of mean JJA surface air temperatures averaged over the eastern United States (100°W-65°W, 31°N-50°N, quadrangle in Fig. 1) with SSTs in spring over 1979-2008 for each AMIP model. The dashed contour lines enclose regions in which the correlations are statistically significant ($p < 0.05$). All data are detrended by subtracting the 7-year moving averages. We use the ensemble member r1i1p1 for each model.

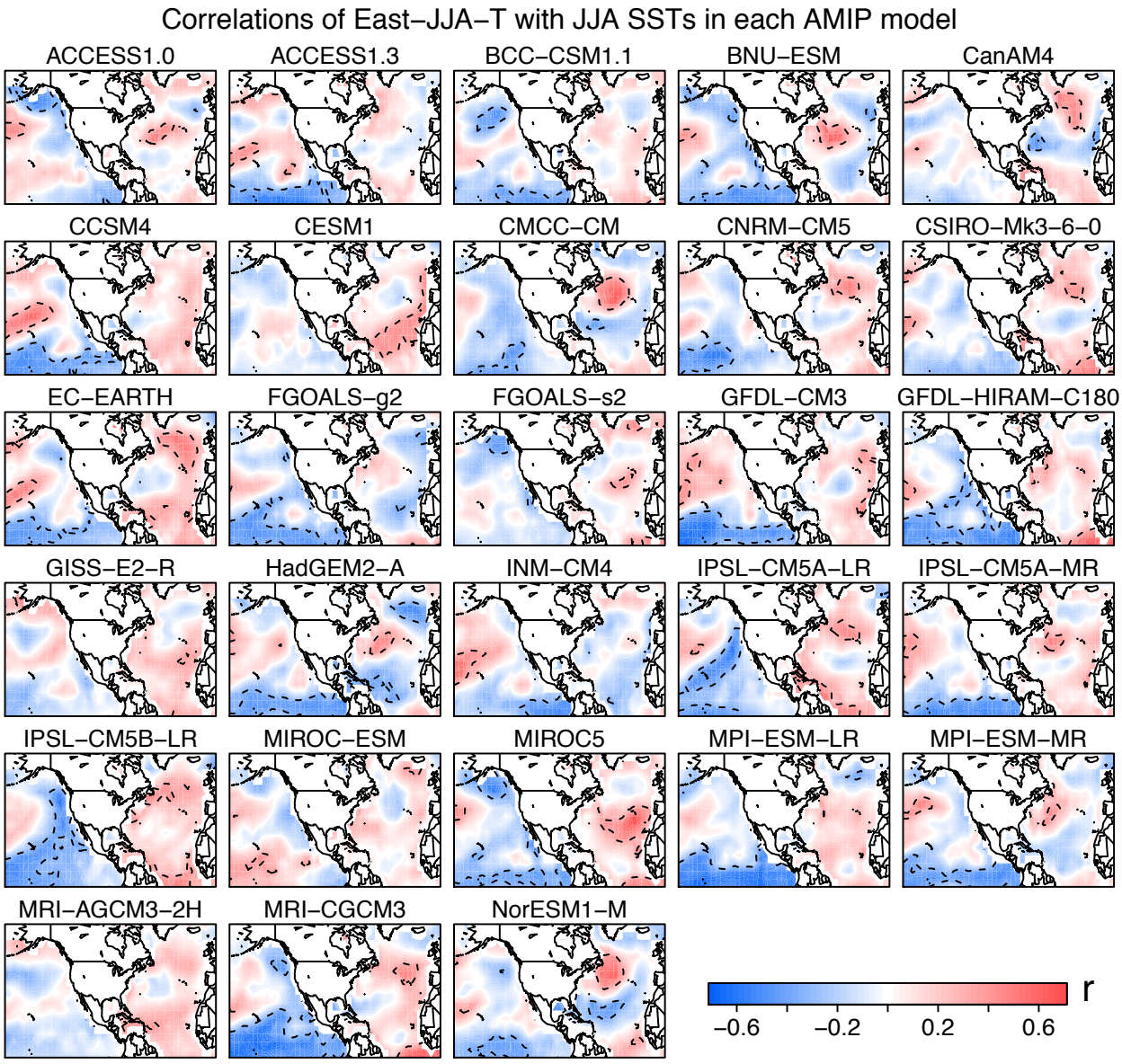

Fig. S13. Correlations of mean JJA surface air temperatures averaged over the eastern United States (100°W-65°W, 31°N-50°N, quadrangle in Fig. 1) with SSTs in summer over 1979-2008 for each AMIP model. The dashed contour lines enclose regions in which the correlations are statistically significant ($p < 0.05$). All data are detrended by subtracting the 7-year moving averages. We use the ensemble member r1i1p1 for each model.

12. EOF analysis of summertime surface air temperature from 1979 to 2008

We apply EOF analysis to test the skills of individual AMIP models in simulating spatial-temporal temperature variability. We proceed as follows. Using the NCEP Reanalysis, we first calculate the EOFs of JJA surface air temperature over North America and surrounding oceans for 1979-2008, as shown in Fig. S14. The first EOF pattern, explaining 22.8% of the total variance, shows a positive anomaly expanding from tropical Atlantic and Pacific to the eastern North America and a negative anomaly in the western United States and central Pacific. The second EOF pattern, explaining 18.3% of the total variance, displays a bimodal structure with positive anomaly in the eastern Pacific and negative anomaly in the North America and northern Atlantic. In the AMIP models, the first two EOF patterns in JJA surface temperatures generally resemble those observed (Fig. S15-16). But the AMIP EOF1 patterns display a range of anomalies from negative to positive in the eastern United States (Fig. S15), while the observed EOF1 is uniformly positive there (Fig. S14). Then we calculate the time series of the two principal components, PC1 and PC2, for the 20th Century Reanalysis and for each model by projecting the temperature fields onto the constructed EOF basis. For the AMIP models, this is written as

$$PC1_k = T_k \bullet EOF1$$
$$PC2_k = T_k \bullet EOF2$$

where T is the mean JJA temperature and k in an index of the AMIP models. We then compare the standard deviations of the PC vectors in the 20th Century Reanalysis and in each AMIP model to those in NCEP. Fig. S17 reveals that all models show less temporal variability in both EOF1 and EOF2, suggesting that the AMIP models cannot fully reproduce the observed EOF patterns of summertime temperature over North America and surrounding oceans.

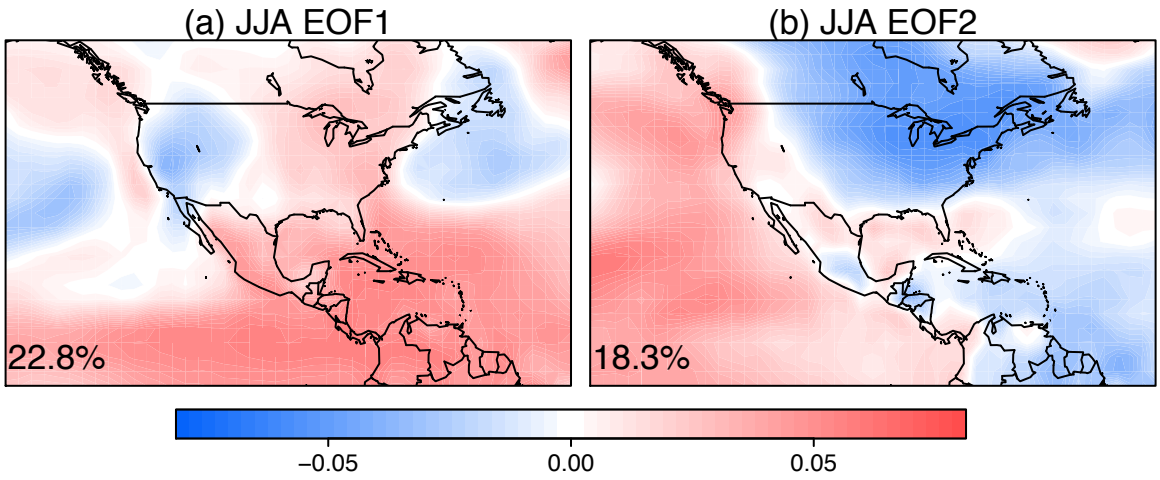

Fig. S14. The first two EOF patterns of mean JJA surface air temperature for 1979-2008. Before performing EOF analysis, we scale the time series of temperature in each grid box to achieve zero mean and unit standard deviation. The variances in surface temperature explained by each EOF mode are shown inset.

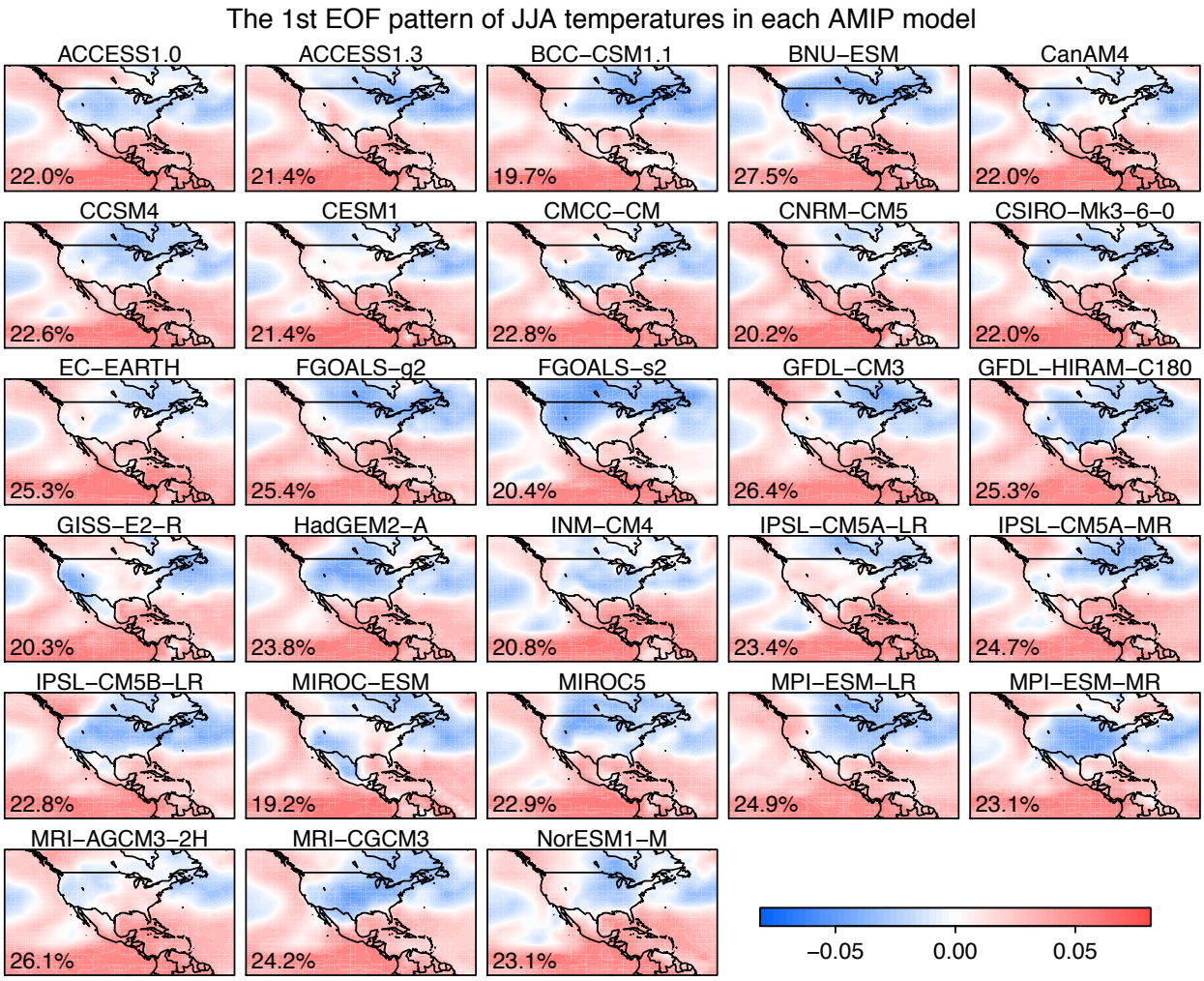

Fig. S15. The first EOF pattern of mean JJA surface air temperatures over 1979-2008 in each AMIP model. Before performing EOF analysis, we scale the time series of temperature in each grid box to achieve zero mean and unit standard deviation. The variances in surface temperature explained by each EOF mode are shown inset.

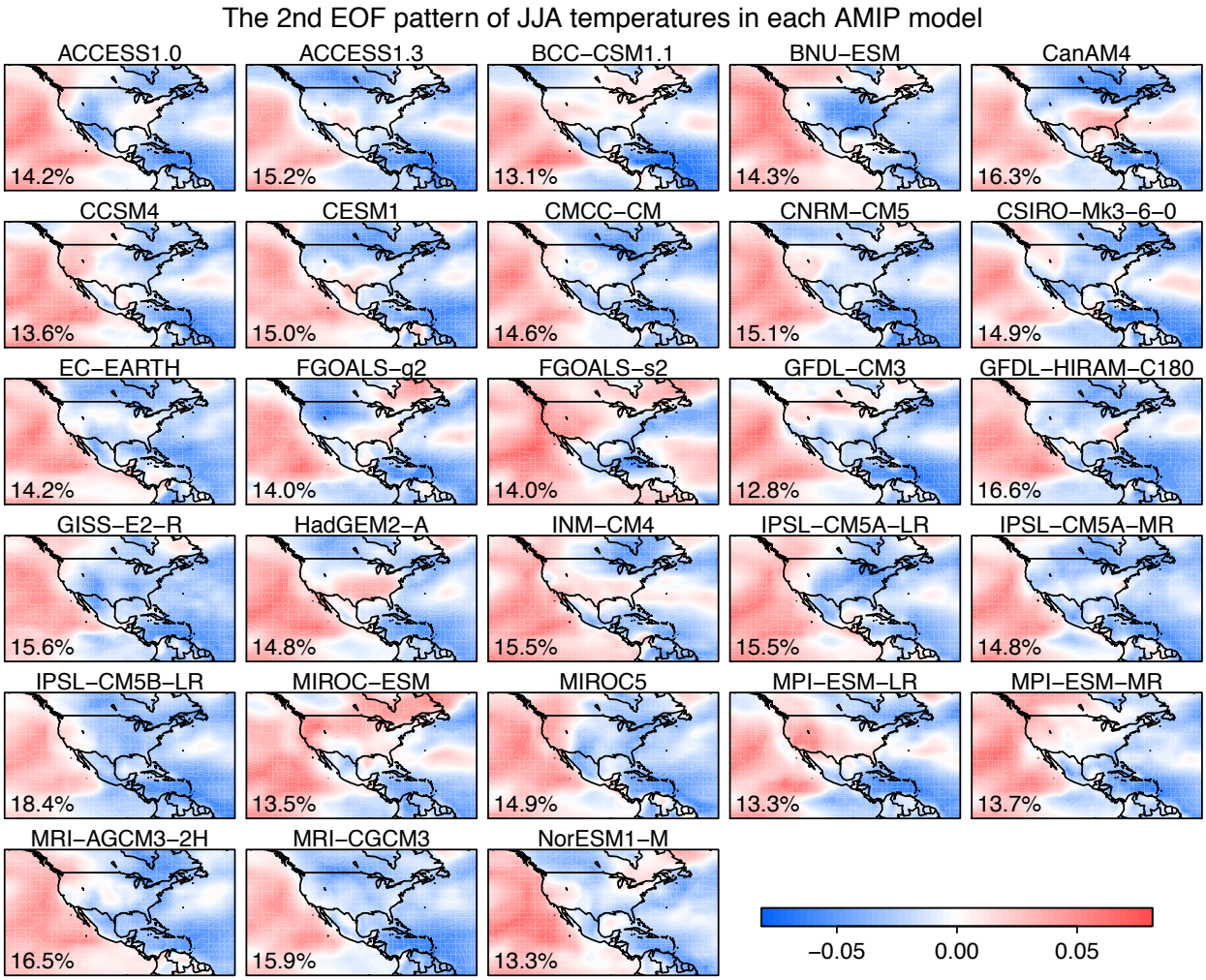

Fig. S16. Similar as Fig. S15, but for the second EOF pattern.

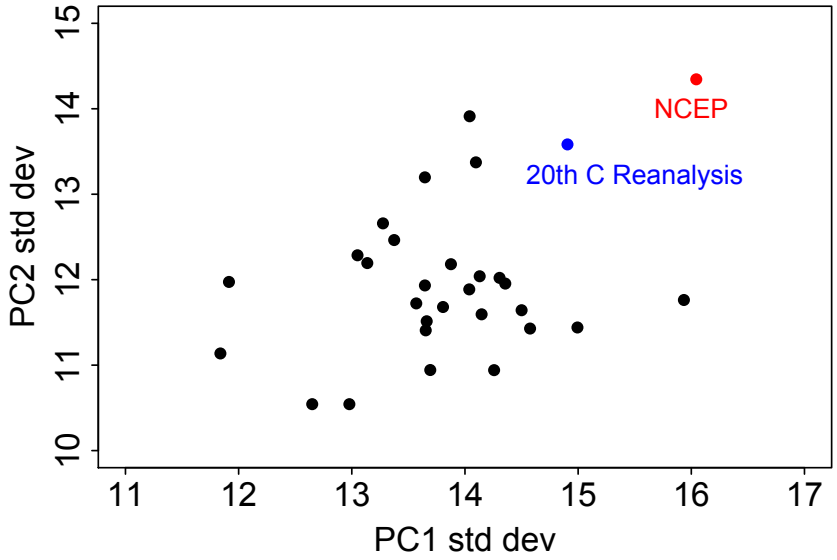

Fig. S17. Standard deviations (std dev) of the time series of the two principal components (PC1 and PC2) in the NCEP reanalysis, 20th Century Reanalysis, and AMIP model ensemble. Each black dot represents results from one AMIP model. See text for more details.

13. Correlation of summertime surface temperatures in the eastern United States and SLP.

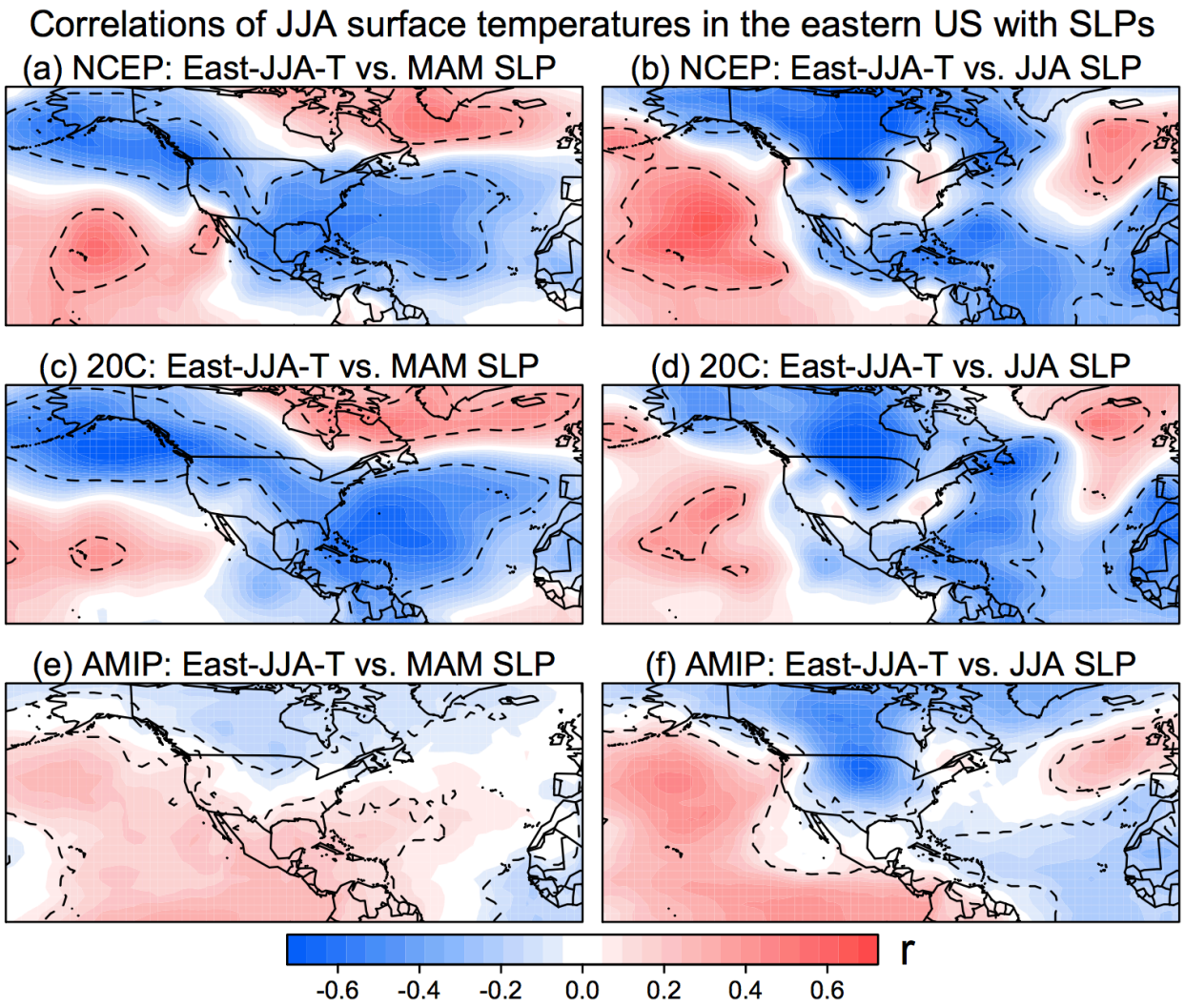

Fig. S18. Same as Fig. 5, but for SLP.

14. Influence of tropical Atlantic SSTs on surface temperatures in the eastern United States.

To create an idealized representation of the Atlantic Multidecadal Oscillation (AMO) for simulations in the GISS ModelE2, we rely on the HadISST SST dataset and proceed as follows. We first remove high-frequency fluctuations in the 1900-2012 timeseries of annual mean global SSTs outside the North Atlantic (0-60°N, 75°W-7.5°W) by applying a low-pass filter. More specifically, we use locally-weighted scatterplot smoothing (Lowess) with a smoothing parameter of 2/3 (8). We next define an AMO index as the annual mean difference between average North Atlantic SSTs and average low-pass-filtered SSTs elsewhere, as in Sutton et al. (9). We standardize the AMO index to zero mean with variance $\pm$ 1.0 and further smooth the AMO timeseries by applying an 11-year moving average. Following Sutton et al. (3, 4), we then regress the 1900-2012 annual mean SSTs in each gridbox onto the standardized and smoothed AMO index, yielding the SST sensitivity to a unit change of AMO (Fig. S19a). We apply this regression only to those gridboxes within the tropical Atlantic (0-30°N), the region we show has a strong influence on U.S. surface temperatures. This procedure produces a map of SST anomalies in the tropical Atlantic associated with the positive phase of an idealized AMO. Simply reversing the sign of the anomalies yields the SST pattern associated with the negative phase of an idealized AMO.

As in Sutton et al. (3, 4), we scale the resulting patterns of positive and negative mean AMO SSTs by a factor of 4 and apply these patterns to the GISS ModelE2. The scaling allows the climate model to reach equilibrium with a shorter integration time. We define TA^+ as the simulations representing the positive AMO phase, and TA^- as the simulations representing the negative AMO phase, based on the 1900-2012 climatological mean SST. The model is integrated for 21 years with the first year discarded. To achieve a realistic outcome, we rescale the modeled surface temperatures anomalies over land by 1/4.

The leading SST patterns in the CLIVAR experiments are calculated using rotated empirical orthogonal functions (EOFs) with varimax rotations (10). The third EOF pattern of global SST in this study is mainly confined to the north Atlantic Ocean and resembles the AMO pattern in Sutton et al. (3, 4) as well as the one we used to drive GISS ModelE2. We focus on the simulations forced by the SST anomaly in the tropical Atlantic (88°W-13°W and 12°N-18°N), as in Schubert et al. (10). Outside the tropical Atlantic, this SST anomaly tapers linearly and becomes zero at 6°N and 24°N (Fig. S20a). The region covered by this SST anomaly is smaller that that in Sutton et al. (3, 4) and what we apply to the GISS ModelE2 (Fig. S19a). The TA^+ and TA^- simulations were integrated for 51 years with these idealized positive and negative SST anomaly patterns (10). Because no TA^- simulation exists for NCAR CAM3.5, we show the difference of TA^+ and the control simulation (neutral Atlantic Ocean) for this model.

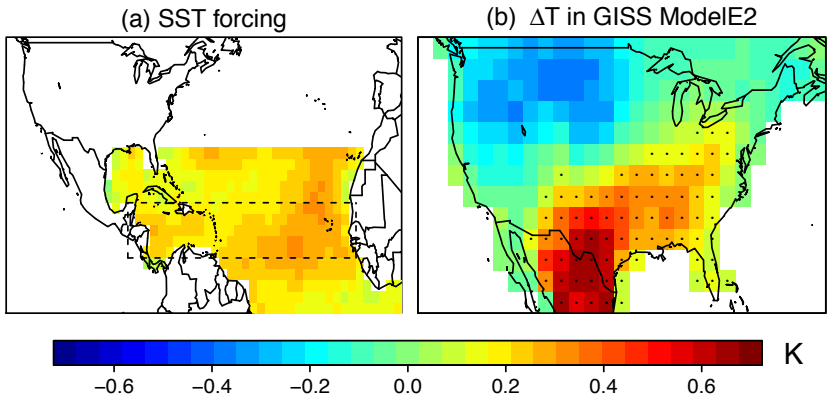

Fig. S19. (a) The perturbation in SSTs used to drive ModelE2 (TA^{+} - TA^{-}). This pattern in SST warming is typical of positive AMO conditions, with an average warming of 0.25 K in the region enclosed by the rectangle (88°W-13°W, 10°N-20°N). (b) Simulated response in JJA surface air temperatures to warming of the tropical Atlantic (panel a) in ModelE2. Gridboxes with statistically significant temperature changes are stippled ($p < 0.05$).

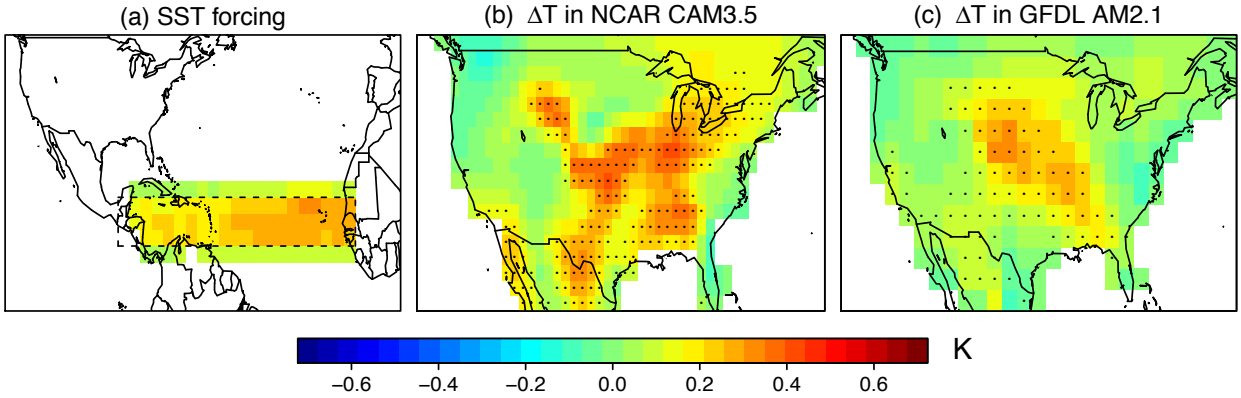

Fig. S20. (a) The perturbation in sea surface temperatures used to drive the CLIVAR models. The average warming in the region enclosed by the rectangle (88°W-13°W, 10°N-20°N) is 0.25 K. (b-c) Simulated response in JJA surface air temperatures to warming of the tropical Atlantic (panel a) in NCAR CAM3.5 and GFDL AM2.1. Gridboxes with statistically significant temperature changes are stippled ($p < 0.05$).

15. Correlations of summertime ozone in the eastern United States with SSTs/SLPs in the high-NOx and low-NOx timeframe.

Anthropogenic NOx emissions in the United States have been decreasing since the 1980s, with the fastest decrease occurring since 2003 (Fig. S21). An unanswered question is whether these emission changes will affect the correlations of summertime ozone in the eastern United States with large-scale meteorological patterns. More specifically, will the predictability of seasonal ozone increase or decrease in the cleaner environment of the future?

To address this question, we calculate the correlations of summertime ozone in the eastern United States with SSTs in the leading months over the high-NOx (1980-1996) and low-NOx (1997-2013) time periods. In both periods, high ozone concentrations are associated with a warm northern tropical Atlantic and cool northeastern Pacific (Fig. S22a-b), consistent with Fig. 1. However, correlations with tropical Atlantic SSTs decrease from 1980-1996 to 1997-2013 (Fig. S22a-b), suggesting reduced seasonal ozone predictability in recent decades. Unlike ozone, JJA surface temperatures in the eastern United States show strong dependence on tropical Atlantic and northeast Pacific SSTs in both timeframes (Fig. S22c-d). Does this mean the relationship of ozone and temperature has weakened in a cleaner environment? Fig. S23 displays the correlation of summertime ozone and temperature in the East. In the more recent decade, these correlations strengthen across the East and the region with significant correlations expands. This result implies that the decline in ozone predictability in Fig. S22 does not arise from reduced sensitivity of temperature in the eastern United States to SSTs, but from some other process.

Using SLPs instead of SSTs, we repeat this correlation analysis over the high-NOx and low-NOx time periods, finding that the correlation patterns remain largely unchanged between the two periods (Fig. S24). Given the relatively short time periods considered here (17 years) and the contrasting results using SSTs and SLPs, we cannot yet with confidence diagnose a trend in ozone predictability.

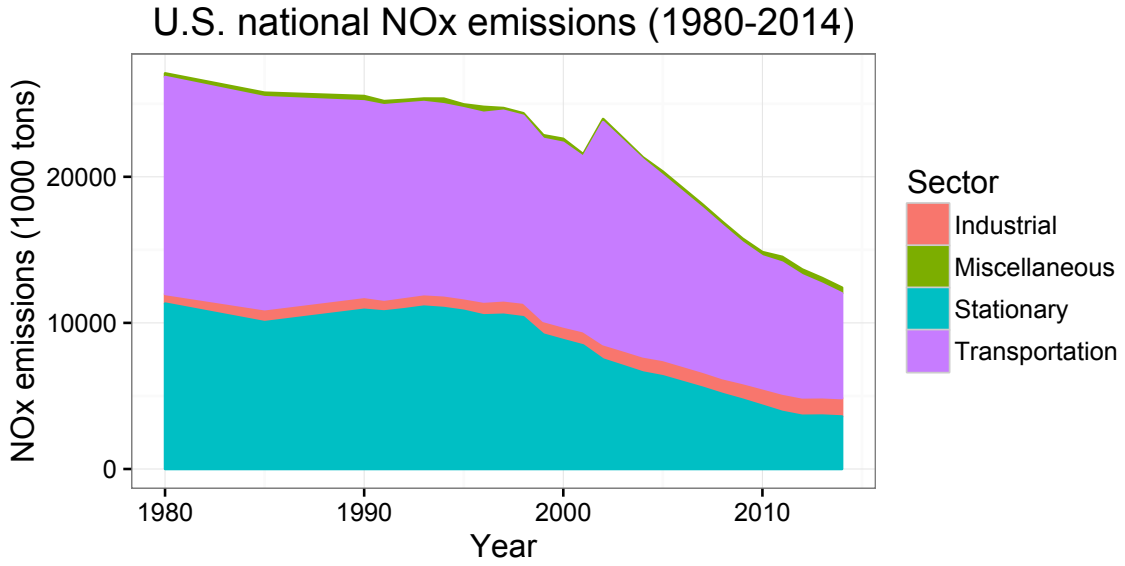

Fig. S21. U.S. anthropogenic NOx emissions from 1980 to 2014. Data are from the U.S. Environmental Protection Agency (https://www.epa.gov/air-emissions-inventories/air-pollutant-emissions-trends-data).

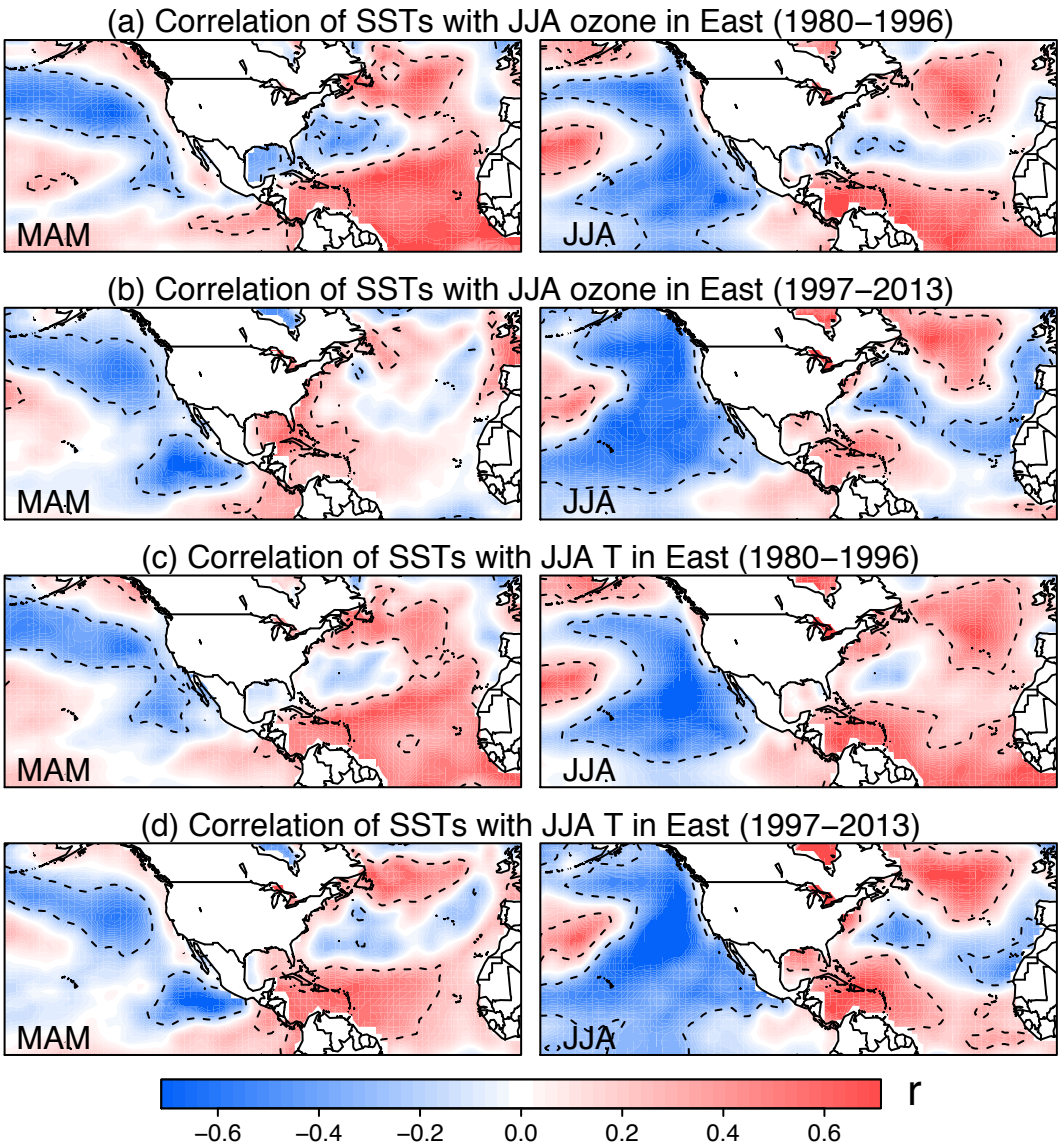

Fig. S22. Correlations of JJA MDA8 ozone in the eastern United States with seasonal mean SSTs in MAM and JJA over two time periods with (a) high NOx (1980-1996) and (b) low NOx (1997-2013) emissions. Panels c-d are the same as panel a-b, but for JJA surface temperatures in the East. Dashed contour lines enclose regions in which the correlations reach statistical significance ($p < 0.10$).

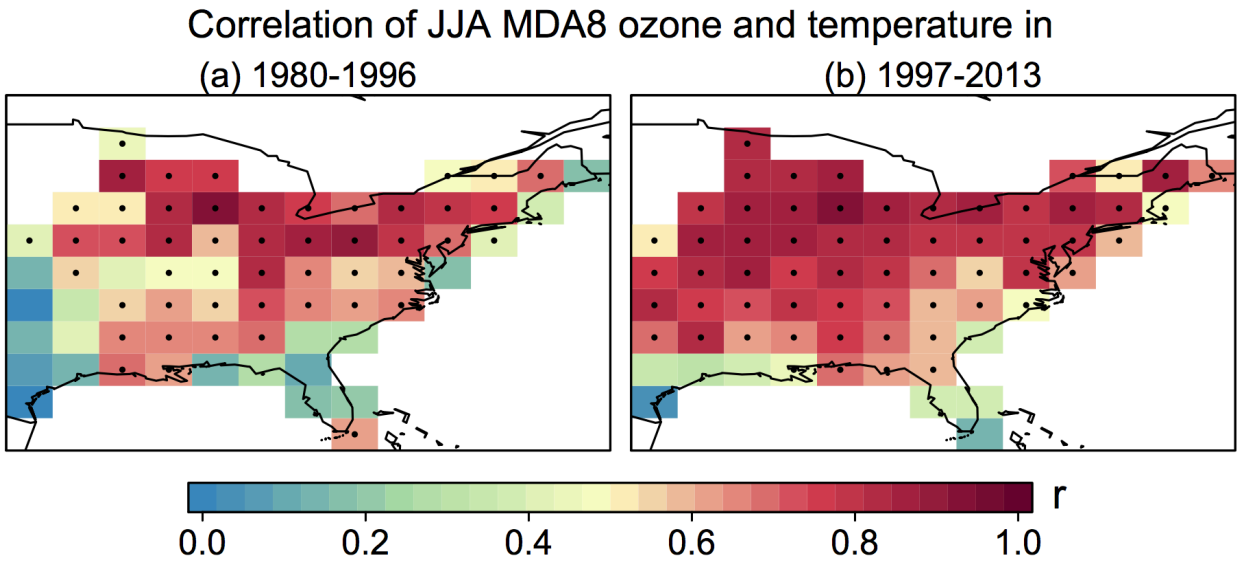

Fig. S23. Correlations of JJA MDA8 ozone and surface temperatures in (a) 1980-1996 and (b) 1997-2013.

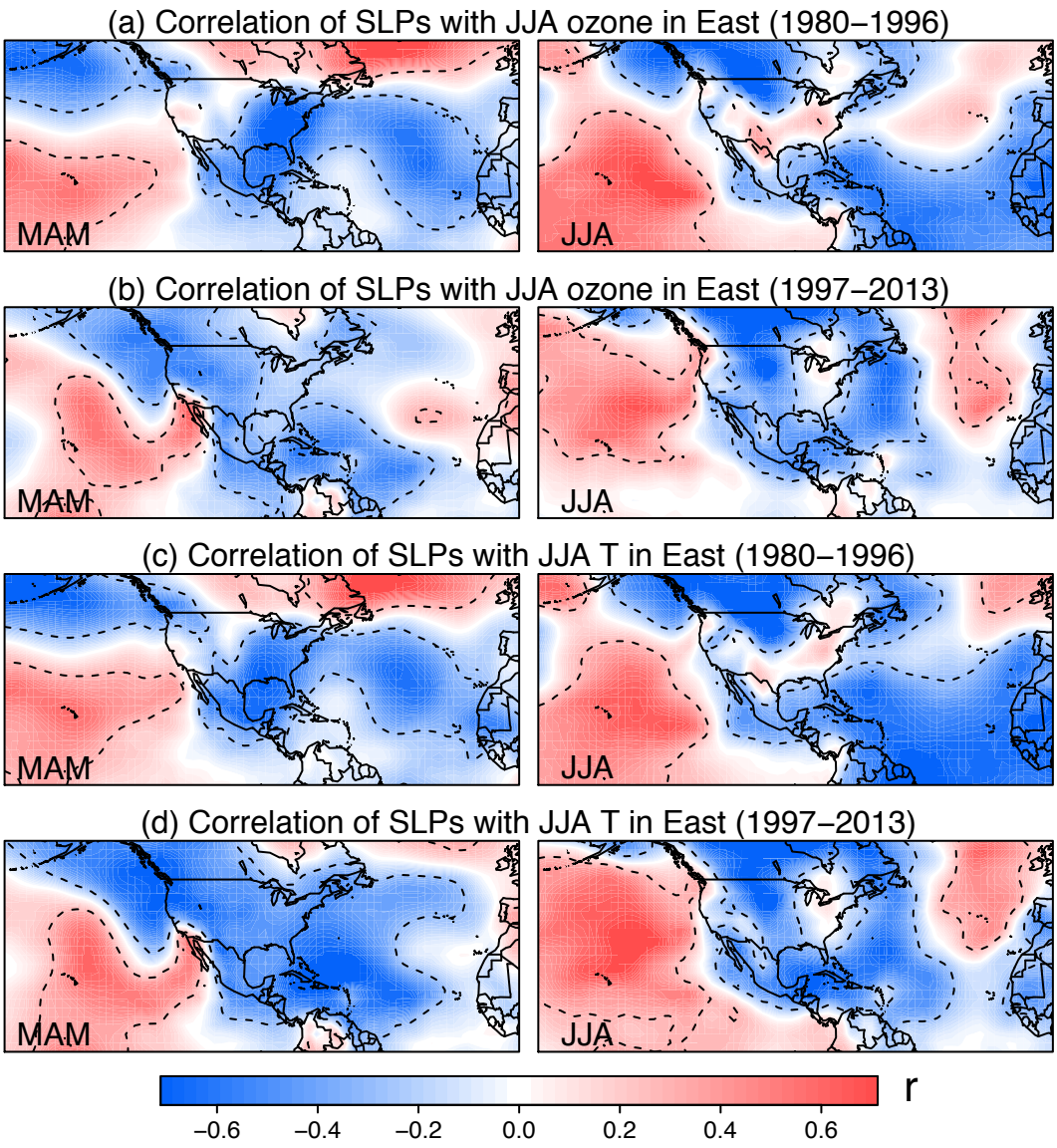

Fig. S24. Similar with Fig. S22, but for the correlations of JJA MDA8 ozone in the eastern United States with seasonal mean SLPs.

16. Non-linear ozone trend from 1980 to 2013 and the choice of detrending method in quality planning

Figure S25a displays the non-linear summertime ozone trends in the eastern United States from 1980 to 2013. Average MDA8 ozone concentrations decrease at a relatively slow rate of -0.065 ppbv a^{-1} from 1980 to 2002, compared to a much faster rate of -0.486 ppbv a^{-1} from 2002 to 2013. This abrupt change is caused by the rapid decrease of ozone precursors since 2002 (11), as seen from Fig. S21. To remove this non-linear trend, detrended data and anomalies are obtained using two different approaches. Using a 7-year moving average (MA) to detrend the timeseries yields a correlation coefficient *r* of 0.59 between observed and predicted ozone. Using a 7-term Henderson Filtered (HF) averaged can yield a higher correlation coefficient of 0.67. However, these two centered moving average approaches cannot be used in practical air quality planning because they require ozone concentrations in both the past and future years. However, we can still obtain good ozone predictability if an appropriate assumption of the ozone trend is made. For example, if we detrend the timeseries by subtracting the quadratic fitted (QF) trend, as suggested by Fig. S25a and Figure S21, the correlation coefficient of observed and predicted ozone is 0.59 (Fig. S25b), which matches the value obtained with the 7-year MA approach.

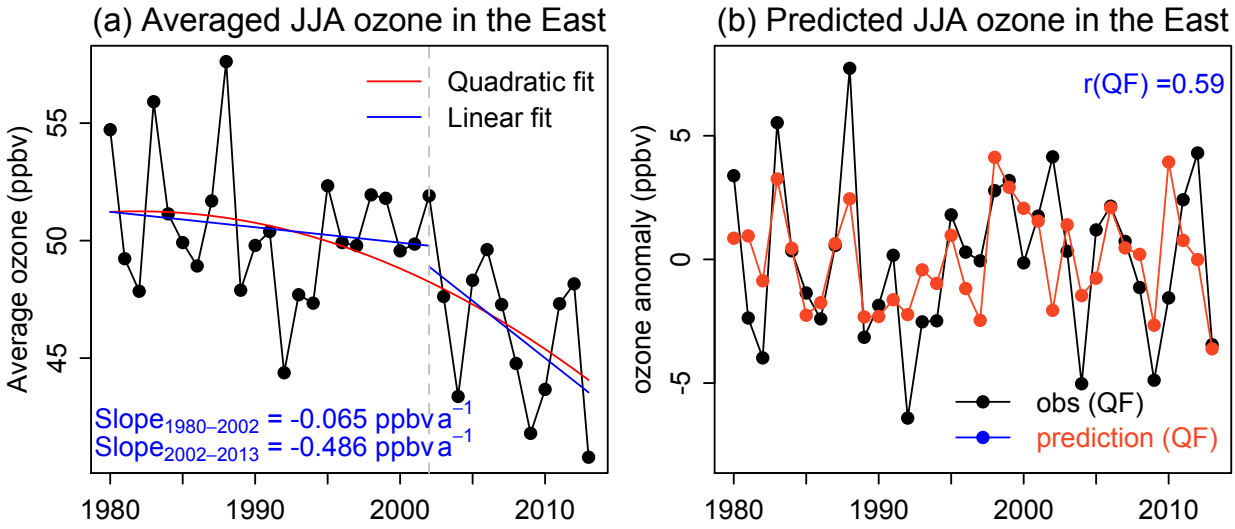

Fig. S25. (a) Timeseries of average JJA MDA8 ozone concentrations in the eastern United States. The red curve denotes the quadratic fitted (QF) trend of this timeseries. The blues lines denote the linear fit of this timeseries in the timeframe 1980-2002 and 2002-2013. The slopes are shown inset. (b) Same as Fig. 3, but here the detrended ozone concentrations and meteorology are obtained by subtracting the quadratic fitted trend.

17. Comparison of detrending methods

Figure S26 displays the detrended JJA MDA8 ozone concentration in the eastern United States by subtracting the 7-year moving average (MA), the 7-term Henderson filter (HF), and the quadratic fitted (QF) trends. The Henderson filter relies on a weighted moving average and assumes the trends follows a local cubic polynomial, which can better damp irregular changes (12), as seen in Fig. S26. The standard deviation of detrended timeseries is 2.31 ppbv using HF, compared to 3.15 ppbv using MA and 3.20 ppbv using QF.

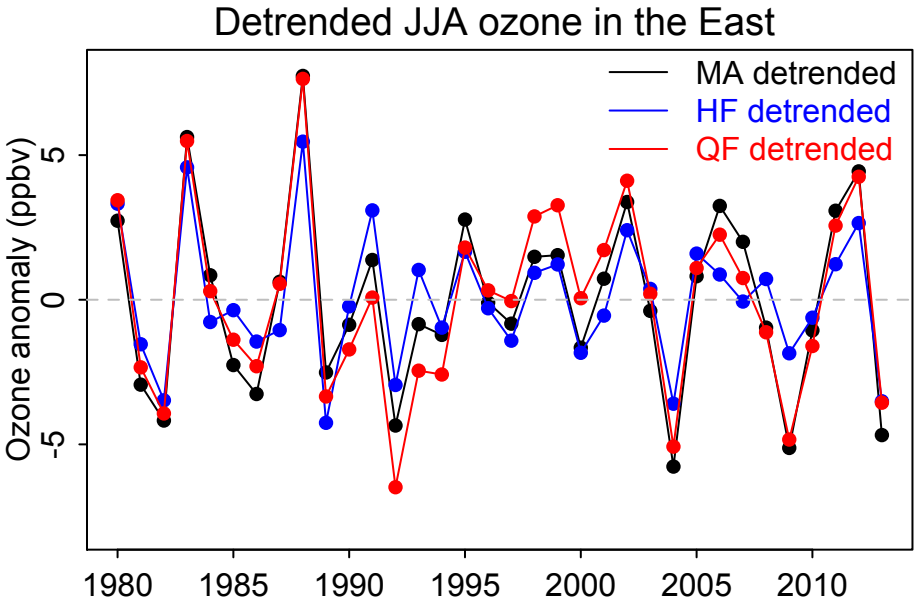

Fig. S26. Timeseries of detrended JJA MDA8 ozone concentrations averaged over the eastern United States using different detrending methods, including subtracting the 7-year moving average (MA), the 7-term Henderson filter (HF) and the quadratic fitted (QF) trends.

References

1. Xie P, et al (2007) A gauge-based analysis of daily precipitation over East Asia. J Hydrometeorol, 8(3): 607-626.
2. Chen M et al. (2008) Assessing objective techniques for gauge-based analyses of global daily precipitation. J Geophys Res Atmos, 113(D4).
3. Sutton RT, Hodson DL(2005) Atlantic Ocean forcing of North American and European summer climate. Science, 309(5731): 115-118.
4. Sutton RT, Hodson DL (2007) Climate response to basin-scale warming and cooling of the North Atlantic Ocean. J Climate, 20(5): 891-907.
5. Johnstone JA, Mantua NJ (2014) Atmospheric controls on northeast Pacific temperature variability and change, 1900–2012. Proc Natl Acad Sci, 111(40): 14360-14365.
6. Bond NA, Cronin MF, Freeland H, Mantua N (2015) Causes and impacts of the 2014 warm anomaly in the NE Pacific. Geophys Res Lett, 42(9): 3414-3420.

7. McKinnon KA, Rhines A, Tingley MP, Huybers P (2016) Long-lead predictions of eastern United States hot days from Pacific sea surface temperatures. Nat Geosci, 9(5).
8. Cleveland WS (1981) LOWESS: A program for smoothing scatterplots by robust locally weighted regression. Am Stat, 35(1).
9. Sutton RT, Dong B (2012) Atlantic Ocean influence on a shift in European climate in the 1990s. Nat Geosci, 5(11): 788-792.
10. Schubert S, et al. (2009) A US CLIVAR project to assess and compare the responses of global climate models to drought-related SST forcing patterns: overview and results. J Climate, 22(19): 5251-5272.
11. Bloomer BJ, Stehr JW, Piety CA, Salawitch RJ, Dickerson RR (2009) Observed relationships of ozone air pollution with temperature and emissions. Geophys Res Lett, 36: L09803.
12. Australian Bureau of Statistics (2003) Information Paper: A Guide to Interpreting Time Series - Monitoring Trends. Australian Bureau of Statistics, cat. 1349.0, Canberra, Australia.